

Gas and dust hydrodynamical simulations of massive lopsided transition discs – II. Dust concentration

Clément Baruteau^{1*} and Zhaohuan Zhu^{2,3}

¹*CNRS / Institut de Recherche en Astrophysique et Planétologie, 14 avenue Edouard Belin, 31400 Toulouse, France*

²*Department of Astrophysical Sciences, 4 Ivy Lane, Peyton Hall, Princeton University, Princeton, NJ 08544, USA*

³*Hubble Fellow*

Accepted 2015 October 27. Received 2015 October 27; in original form 2015 August 4

ABSTRACT

We investigate the dynamics of large dust grains in massive lopsided transition discs via 2D hydrodynamical simulations including both gas and dust. Our simulations adopt a ring-like gas density profile that becomes unstable against the Rossby-wave instability and forms a large crescent-shaped vortex. When gas self-gravity is discarded, but the indirect force from the displacement of the star by the vortex is included, we confirm that dust grains with stopping times of order the orbital time, which should be typically a few centimetres in size, are trapped ahead of the vortex in the azimuthal direction, while the smallest and largest grains concentrate towards the vortex centre. We obtain maximum shift angles of about 25 degrees. Gas self-gravity accentuates the concentration differences between small and large grains. At low to moderate disc masses, the larger the grains, the farther they are trapped ahead of the vortex. Shift angles up to 90 degrees are reached for 10 cm-sized grains, and we show that such large offsets can produce a double-peaked continuum emission observable at mm/cm wavelengths. This behaviour comes about because the large grains undergo horseshoe U-turns relative to the vortex due to the vortex's gravity. At large disc masses, since the vortex's pattern frequency becomes increasingly slower than Keplerian, small grains concentrate slightly beyond the vortex and large grains form generally non-axisymmetric ring-like structures around the vortex's radial location. Gas self-gravity therefore imparts distinct trapping locations for small and large dust grains which may be probed by current and future observations, and which suggest that the formation of planetesimals in vortices might be more difficult than previously thought.

Key words: accretion, accretion discs — hydrodynamics — instabilities — methods: numerical — planetary systems: protoplanetary discs

1 INTRODUCTION

Transition discs are protoplanetary discs around young (1–10 Myr) stars with little or no emission in the near- and mid-IR but strong emission at longer wavelengths (see the review by [Espaillat et al. 2014](#)). Modeling of the Spectral Energy Distribution (SED) of transition discs implies that their inner parts form dust cavities largely devoid of small dust grains, followed by cold dust populating an outer disc. Interferometric imaging shows that the cavities also have a deficit in (sub-)mm continuum emission and are mostly devoid of large dust grains. Cavities typically span a few tens of Astronomical Units (AU) like in LkCa 15 (~50 AU; [Andrews et al. 2011b](#)) and AB Aur ($\gtrsim 70$ AU; [Piétu et al. 2005](#)), with minimum and maximum sizes so far in TW Hya (~4 AU; [Hughes](#)

[et al. 2007](#)) and HD 142527 (~140 AU; [Casassus et al. 2013; Avenhaus et al. 2014](#)). A subset of transition discs shows significant near-IR excesses. These so-called pre-transition discs feature an optically thick inner disc of typically ~1 AU between the star and the cavity, and some of them have accretion rates exceeding a few $\times 10^{-8} M_{\odot} \text{ yr}^{-1}$ ([Espaillat et al. 2014](#), and references therein). There is growing observational evidence that gas is present in the dust cavities of (pre-)transition discs, though at a reduced level compared to the outer disc ([Carmona et al. 2014; Bruderer et al. 2014](#)). The decrease in gas surface density inside the cavity varies from 1 to 4 orders of magnitude ([van der Marel et al. 2015](#)).

Several origins for the diversity of cavity sizes and accretion rates have been explored. One is grain growth and the consequent decrease in the dust emissivity: cavities would be only apparent. In the inner disc, however, grain growth is shown to be limited by destructive collisions to mm/cm particles, which should be detected in the sub-mm. It there-

* E-mails: clement.baruteau@irap.omp.eu (C.B.); zhzhu@astro.princeton.edu (Z.Z.)

fore appears difficult for fragmentation-limited grain growth to simultaneously account for the near-IR dip in the SED of transition discs and their deficit in sub-mm continuum emission (Birnstiel et al. 2012). Alternatively, large dust and gas cavities could be cleared via photoevaporative winds. A broad range of accretion rates is expected depending on the level of high-energy stellar radiation (extreme UV and X-Ray), consistent with the diversity of accretion rates observed in transition discs (see the review by Alexander et al. 2014). However, current models of photo-evaporation cannot account for discs with both large cavities ($\gtrsim 10$ AU) and substantial accretion rates ($\gtrsim 10^{-9} M_{\odot} \text{ yr}^{-1}$; Owen et al. 2011), nor discs with moderate drops in the gas surface density within the cavity.

A third mechanism for sculpting the cavities of transition discs is dynamical clearing by one or several companions. These can be stellar companions. For example, Casasus et al. (2015a) describe how a highly mutually inclined stellar companion to HD 142527 can generate the fast radial flows inside the cavity of its transition disc (Rosenfeld et al. 2014). These fast radial flows could explain how disc holes could be simultaneously transparent and still contain material that accretes at rates $\gtrsim 10^{-9} M_{\odot} \text{ yr}^{-1}$ (Rosenfeld et al. 2014). Companions can also be planets. The salient point is that the size of the gap opened by a massive planet differs in the gas and in the dust. Gaps in the gas are narrow. For example, for a Jupiter-mass planet orbiting a Solar-mass star, the half-width of the gap does not exceed $\sim 40\%$ of the star-planet separation, even in discs with very low turbulent activity (Crida et al. 2006). Gaps in the dust depend on the size of the dust particles or, more generally, on the coupling between dust and gas (quantified by the Stokes number, see Section 2.2). Dust grains up to few tens of microns are tied to the gas, so the width of their gap is basically the same as the gas (Paardekooper & Mellema 2004; Fouchet et al. 2007; Zhu et al. 2012). Dust in the mm/cm range, however, is not tied to the gas and drifts generally inward as a result of gas friction. Radial drift can, however, stall at locations known as dust traps where the gas pressure is maximum (e.g., Pinilla et al. 2012; Johansen et al. 2014). Simulations of disc-planet interactions show that the outer edge of a planet gap is generally a robust pressure maximum while the inner edge is not: large dust grains initially beyond the planet's orbit can be trapped efficiently at the gap's outer edge while the large dust grains initially inside the planet's orbit migrate inward (e.g., Zhu et al. 2012, 2014). This implies that a single massive planet could simultaneously carve a large cavity in mm-grains and a narrow gap in μm -grains, with therefore no or limited impact on the accretion rate. Large cavities in μm -grains and strong reductions in the accretion rate are not natural outcomes of disc-planet interactions, though they can be obtained by invoking several massive planets in the disc (Zhu et al. 2011).

Recent high-resolution interferometric imaging (especially with ALMA) has highlighted that the mm emission rings of transition discs are often non-axisymmetric. Several of them feature large-scale lopsided structures with distinct crescent or horseshoe shapes. These include HD 142527 (Casassus et al. 2013; Fukagawa et al. 2013), Oph IRS 48 (van der Marel et al. 2013), AB Aur (Tang et al. 2012), SR21 (Andrews et al. 2011a; Pérez et al. 2014), LkH α 330 (Isella et al. 2013) and HD 135344B (Brown et al. 2009; Pérez et al. 2014). Intensity variations along the lopsided rings are by factors of ~ 2 -3 for SR21, LkH α , AB Aur and

HD 135344B, ~ 30 for HD 142527 and >100 for Oph IRS 48. In contrast, the gas emission is generally more symmetric along the lopsided rings (van Dishoeck et al. 2015). These findings are so far best explained by the presence of a long-lived vortex in the gas that would efficiently trap mm-grains.

Probably the most promising vortex-forming instability in the context of lopsided transition discs is the Rossby-Wave Instability (RWI, Lovelace et al. 1999). It is essentially the form of the Kelvin-Helmholtz instability in a differentially rotating disc, and a thin-disc version of the Papaloizou-Pringle instability (Papaloizou & Pringle 1984). It is a linear instability associated with a radial minimum in the gas potential vorticity which, in practice, can be triggered where the pressure has a radial maximum. This may occur (i) near the disc's centrifugal radius due to mass infall from the protostellar cloud (Bae et al. 2015), (ii) at the outer edge of a gap-opening planet (e.g., Lyra et al. 2009; Lin 2012), (iii) at the edges between magnetically active and inactive (dead) regions (e.g., Varnière & Tagger 2006; Regály et al. 2012; Faure et al. 2014; Lyra et al. 2015; Flock et al. 2015), or (iv) at the edge of a disc undergoing photo-evaporation, though to our knowledge this latter scenario has not been examined yet. The planet gap scenario has received the most attention, but detailed modeling is still needed to reproduce observed distributions of gas and dust, like in the Oph IRS 48 disc (Zhu & Stone 2014). The dead/active regions scenario needs more exploration, in particular to determine the efficiency of non-ideal magneto-hydrodynamic effects at suppressing the magneto-rotational instability in the outer regions of transition discs (Lesur et al. 2014; Bai 2015; Gressel et al. 2015).

Another route to producing lopsided dust rings in transition discs has been recently examined by Mittal & Chiang (2015). The authors proposed a model where a massive gas disc exhibits a mode with azimuthal wavenumber $m = 1$ and pattern frequency comparable to the disc's Keplerian frequency. Mutual gravitational interactions will cause the star and disc to rotate about their centre-of-mass, which, if the disc is massive enough, can sustain an $m = 1$ perturbation where the gas describes horseshoe-shaped streamlines. Interestingly, Mittal & Chiang (2015) found that dust grains with Stokes numbers around unity, that is with aerodynamic stopping times around the orbital period, are not trapped at the horseshoe centre: they are shifted azimuthally by up to 45 degrees ahead of the horseshoe centre. These should be mm/cm-grains depending on the gas surface density at the vortex's radial location, thus a significant shift of the grains location relative to the horseshoe centre should be detectable via high-resolution interferometry in the (sub-)mm.

Nonetheless, Mittal & Chiang (2015) left un-addressed several important issues. They envisioned an $m = 1$ mode based on the mutual interaction between the lopsided disc and the star, but the trigger was not specified. We propose that it could be the RWI. Also, gas self-gravity was discarded although its acceleration can be as important as, if not larger than, the indirect acceleration imparted by the star. This we show in an accompanying paper (Zhu & Baruteau, submitted, hereafter Paper I), where we present results of hydrodynamic simulations with and without gas self-gravity, with lopsided gas distributions mediated by the RWI. While Paper I deals with gas only, the present paper presents results of simulations with both gas and dust to investigate the concentration of dust grains when varying the mass of the gas disc, with a focus on large disc masses for which gas self-gravity should matter most. The model set-up is de-

scribed in Section 2. Results of simulations are presented in Section 3, first without gas self-gravity in Section 3.1, then with self-gravity in Section 3.2. These results are used to generate synthetic images of dust continuum observations, which are presented in Section 4. Concluding remarks follow in Section 5.

2 MODEL SET-UP

We carried out 2D hydrodynamical simulations using a modified version of the grid-based code FARGO (Masset 2000) called FARGO-ADSG (Baruteau & Masset 2008a,b), which includes optional energy equation and gas self-gravity. The gas model is detailed in Paper I and briefly recalled in Section 2.1. For this work, a particle integrator has been implemented in FARGO-ADSG for the dust. The dust model is described in Section 2.2. Conversion of our results of simulations from code units to physical units follows in Section 2.3.

2.1 Gas

The gas model and the initial conditions of the simulations are chosen to generate a long-lived elongated vortex through the RWI. Specifically, the initial surface density of the gas has a (modified) Gaussian radial profile of the form

$$\Sigma(r, \varphi) = \Sigma_0 \left[10^{-2} + \exp \left\{ -\frac{(r - r_0)^2}{2\sigma^2} \right\} \right] \times \left[1 + 10^{-3} \times \cos \varphi \times \sin \left(\pi \frac{r - r_{\text{in}}}{r_{\text{out}} - r_{\text{in}}} \right) \right],$$

where Σ_0 is a free parameter that varies the disc mass, r_0 is a reference radius that defines the code's unit of length, $\sigma = 2H(r_0)$ with $H = c_s/\Omega_K$ the disc's pressure scale height, c_s the sound speed and Ω_K the Keplerian angular frequency. We take H equal to $0.1r$ and constant in time (the disc is assumed to be isothermal). The second bracket in the above equation corresponds to a small perturbation of azimuthal wavenumber $m = 1$ applied smoothly between the grid's inner edge ($r_{\text{in}} = 0.2r_0$) and outer edge ($r_{\text{out}} = 2r_0$).

The gas disc that we simulate is therefore a narrow ring of gas rather than an extended outer disc beyond a cavity, as is observed in transition discs. This is mainly for numerical convenience, as it allows us to reduce the radial extent of the computational grid that simulates the disc, and to focus on the dynamics of the gas and dust near the vortex. In particular, the low densities at the disc edges minimize edge effects in the direct and indirect contributions to the disc's gravitational potential (Heemskerk et al. 1992; Adams et al. 1989).

The simulations presented in this paper are summarised in Table 1. In the simulations with gas self-gravity, the disc gravitationally accelerates itself and the star, while in the simulations without self-gravity, the disc only accelerates the star. In all the simulations, the star remains at the origin of the reference frame, and the indirect terms that account for the acceleration of the star by the disc are therefore included in the equations of motion, regardless of whether self-gravity is included or not. Our median value $\Sigma_0 = 5 \times 10^{-3}$ corresponds to an initial disc-to-star mass ratio of 1.7%. The Toomre parameter, $Q \approx c_s \Omega / \pi G \Sigma$, with Ω the disc's angular frequency and G the gravitational constant, is initially

Table 1. Simulation models

Name	Gas self-gravity	Σ_0 [code units]
g0p2	Yes	0.2×10^{-3}
g0p5	Yes	0.5×10^{-3}
g2n	No	2×10^{-3}
g2	Yes	2×10^{-3}
g5n	No	5×10^{-3}
g5	Yes	5×10^{-3}
g10n	No	10×10^{-3}
g10	Yes	10×10^{-3}

equal to 13, 5 and 2.5 at $r = r_0$ in models g2, g5 and g10, respectively.

A small turbulent viscosity is included in the simulations. Preliminary runs have shown that a constant alpha viscous parameter $\alpha = 10^{-6}$ is a good compromise between a strong, long-lived vortex (which requires low viscosities, particularly with gas self-gravity as it inhibits the RWI; Goodman & Narayan 1988) and convergence with increasing grid resolution (which would favour large viscosities).

The hydrodynamical equations are solved on a polar grid with $N_r = 300$ cells logarithmically spaced between r_{in} and r_{out} , and $N_s = 600$ sectors evenly spaced between $\varphi = 0$ and 2π . This grid resolution is sufficient for our purposes and helps maintain a tractable computational cost when including many dust particles. Although the logarithmic radial spacing is only required for the Fast Fourier Transform algorithm in the calculation of the gas self-gravity (Baruteau & Masset 2008b), it is also used without self-gravity to keep the same grid resolution in all simulations. When self-gravity is included, a softening length $\varepsilon = 0.3H(r)$ is used in the self-gravitating potential to mimic the effect of a finite vertical thickness. Standard outflow (zero-gradient) boundary conditions are used in the simulations.

2.2 Dust

Dust is modelled by Lagrangian particles that feel the star's gravity (direct and indirect acceleration terms), gas drag, but that do not interact together (no dust self-gravity, no collisions nor growth). An important point is that when gas self-gravity is included, the particles also feel the self-gravitating acceleration of the gas. It implies that differences in the gas and dust velocities are only imparted by the pressure force felt by the gas. We discard possibly important effects of dust feedback onto the gas (e.g., Crnkovic-Rubsamen et al. 2015).

The dust particles that we simulate are much smaller than the molecular mean-free path in our disc models (see Section 2.3). The drag force exerted by the gas therefore corresponds to the so-called Epstein regime, and the particles Stokes number (St), which is a dimensionless measure of the particles stopping time ($\tau_s = \text{St} \Omega^{-1}$), is given by

$$\text{St} = \frac{\pi}{2} \frac{s \rho_{\text{pc}}}{f_{\text{D}} \Sigma_{\text{gas}}} \approx \frac{0.015}{f_{\text{D}}} \times \left(\frac{s}{1 \text{ mm}} \right) \left(\frac{\rho_{\text{pc}}}{1 \text{ g cm}^{-3}} \right) \left(\frac{10 \text{ g cm}^{-2}}{\Sigma_{\text{gas}}} \right) \quad (1)$$

with s the physical radius of the particles, ρ_{pc} their internal mass density (we choose $\rho_{\text{pc}} = 1 \text{ g cm}^{-3}$), Σ_{gas} the gas surface density at the particles location, and $f_{\text{D}} = \sqrt{1 + 9\pi \mathcal{M}^2 / 128}$ is a dimensionless coefficient that features the Mach number of the dust relative to the gas,

$\mathcal{M} = |\mathbf{v} - \mathbf{v}_{\text{gas}}|/c_s$ (Paardekooper 2007, \mathbf{v} and \mathbf{v}_{gas} denote the velocity vector of the dust and gas, respectively). In practice $f_D \approx 1$ in our simulations. We consider several particle sizes that are fixed in the simulations. Thus, the particles Stokes number does vary in the simulations according to the gas surface density at the particles location. Stokes numbers typically range from $\sim 10^{-2}$ to ~ 40 , which allows us to probe different trapping efficiencies via gas drag.

We use 10,000 particles to simulate dust grains of a given size. Their initial distribution is uniform between $r = 0.8r_0$ and $1.2r_0$, unless otherwise stated. Their initial velocities are Keplerian, except in simulations with gas self-gravity, for which the initial azimuthal velocity of the particles includes the gas self-gravitating radial acceleration (much like in disc-planet simulations with self-gravity, see Baruteau & Masset 2008b). The number of dust particles may seem rather small but, as we will see in Section 3, dust particles quickly concentrate at well-defined locations in the disc, either at a single point inside or near the vortex, or along a ring around the vortex's radial location. We find 10,000 particles to be enough to describe the dust's azimuthal density distribution when it forms ring-like structures around the vortex's radial location.

The equations of motion for the dust particles are solved with a leapfrog integrator in polar coordinates. The integrator basically corresponds to the 2D leapfrog integrator in cylindrical coordinates implemented by Zhu et al. (2014) in the code ATHENA. We carried out the various tests described in the Appendix of Zhu et al. (2014) to validate our particle integrator. The particle integration scheme is parallelized with MPI using FARGO's domain decomposition into rings. The timestep used in the integration of the dust particles is identical to that used in the gas equations, it is therefore constrained by the Courant-Frederichs-Levy (CFL) condition specific to FARGO. Test simulations using a fixed timestep, chosen to be shorter than the minimum stopping time of the particles, showed negligible changes to our results. In practice, the effective time step in our simulations is shorter than the particles stopping time.

2.3 Conversion from code to physical units

As mentioned in Section 2.1, the radial location r_0 where the initial gas surface density is maximum defines the code's unit of length. The unit of mass is the mass of the central star, and the unit of time is the Keplerian orbital period at $r = r_0$ divided by 2π . Whenever time is expressed in orbits, it refers to the orbital period at $r = r_0$, which we denote by T_{orb} .

To keep our results as general as possible, we do not specify physical units of length and mass in the simulations, since the gas and dust dynamics are set by dimensionless numbers like the Toomre parameter, the disc-to-star mass ratio or the particles Stokes number. All our results are thus shown in code units, but it is very easy to convert them into physical units. Assuming the mass unit is the Sun's mass and the length unit is 65 AU, our median value for Σ_0 of 5×10^{-3} corresponds to $\approx 10 \text{ g cm}^{-2}$ and $T_{\text{orb}} \sim 500$ yrs. For comparison, the gas surface density at the edge of the ~ 70 AU cavity in the J1604-2130 disc is estimated as $\sim 10 \text{ g cm}^{-2}$, and that at the edge of the ~ 45 AU cavity in the LkCa 15 disc is $\sim 60 \text{ g cm}^{-2}$ (van der Marel et al. 2015). Conversion from Stokes number to dust size is via Eq. (1), using $f_D = 1$. If, for example, dust grains have an internal

density of 1 g cm^{-3} , and that the gas surface density at their location is 10 g cm^{-2} (5×10^{-3} in code units), then $St = 1$ particles correspond to $\approx 6 \text{ cm}$ grains. Using the same units, the largest particles that we have simulated are a few metres in size, which remains much smaller than the minimum molecular mean free path in our disc models (~ 300 metres in models g10 and g10n) and justifies that the dust grains that we simulate are in the Epstein regime.

3 RESULTS

This section describes our results of hydrodynamical simulations, first for models without gas self-gravity in Section 3.1, then for models with self-gravity in Section 3.2. Contrary to Paper I where its effect is examined, the indirect term in the star's acceleration on the gas and dust, due to the displacement of the star by the vortex, is included in all the simulations presented in this paper.

3.1 Models without gas self-gravity

In our models without self-gravity, the RWI quickly sets in and forms a single, elongated vortex in less than 30 orbits that lives over the duration of our simulations (500 orbits). Contours of the gas surface density are displayed at 300 orbits in Figure 1 for models g2n, g5n and g10n from top to bottom in the panels. Cartesian coordinates $\{x, y\}$ are used with the star at the origin. To ease the comparison between the models, the maximum in the gas surface density is set at $y = 0$ in the panels. The vortex's radial location, where the azimuthally-averaged surface density of the gas peaks, can thus be read along the x-axis (it also corresponds to the radial location where the gas pressure is maximum since the disc temperature is uniform).

The first notable result, also shown in Paper I, is that the vortex migrates inward fairly rapidly, at a rate that increases nearly proportionally to the disc's initial surface density: in 300 orbits, the vortex's radial location has decreased by about 15%, 35% and 65% in models g2n, g5n and g10n, respectively. The vortex's migration results from an asymmetric wave emission by the vortex (Paardekooper et al. 2010). Vortex migration is therefore due to pressure torques, not to gravitational torques, at least in the absence of gas self-gravity. The waves emitted by the vortex cannot be seen in the panels of Figure 1 because their density contrast relative to the background disc is smaller than the vortex's, and because the radial profile of the gas density drops rapidly away from the vortex's radial location. The wave that propagates inward from the vortex's radial location carries a negative flux of angular momentum and thus exerts a positive torque on the vortex. Conversely, the wave that propagates outward from the vortex's radial location carries a positive flux of angular momentum and exerts a negative torque on the vortex. In the absence of gas self-gravity, geometrical effects and the radial gradient of surface density favour the outer wave, and the net exchange of angular momentum between the vortex and the disc leads to inward migration of the vortex (Paardekooper et al. 2010). We also notice that the vortex strengthens during its inward migration with both the surface density at the vortex centre and the azimuthal contrast in surface density along the vortex increasing over time. At 300 orbits, the surface density

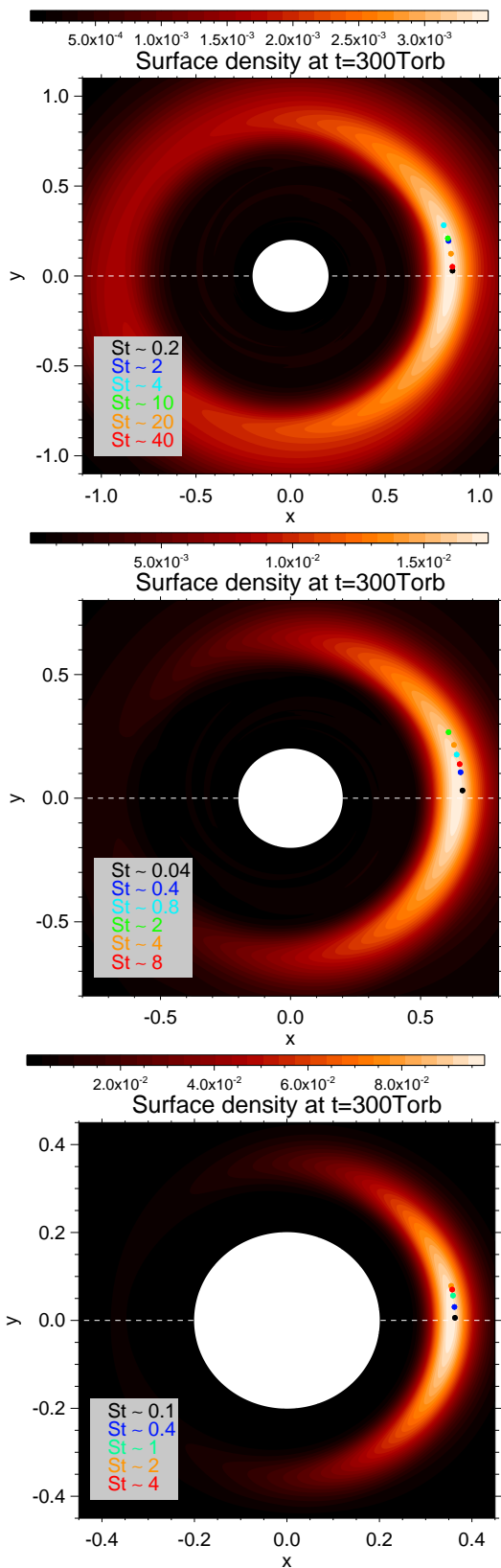


Figure 1. Results of simulations without gas self-gravity for models g2n, g5n and g10n (from top to bottom in the panels). Contours of the gas surface density are shown at 300 orbits. In all panels, the grey dashed line passes by the star and the location in the disc where the gas surface density in the vortex is maximum. The circles filled with different colours show the location of dust particles of various sizes. Their Stokes number at the time of the simulation is indicated in the lower-left corner of the panels.

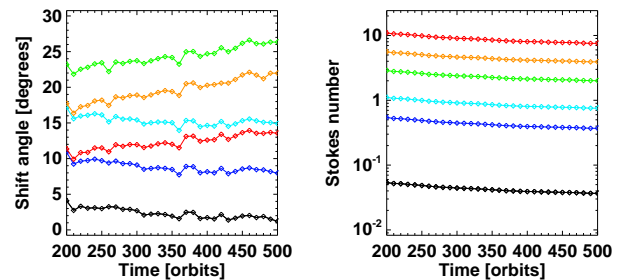


Figure 2. Time evolution of the particles shift angle (left panel) and Stokes number (right panel) in model g5n. Shift angles are defined relative to the location in the vortex where the gas surface density is maximum. The colour of the symbols refers to the same particle size between both panels and is the same as in the middle panel of Figure 1.

contrasts along the vortex are by factors of roughly 2.5, 12 and 25 in models g2n, g5n and g10n, respectively.

The location of the particles is marked by filled circles in Figure 1, with different colours used for different particle sizes. Recall that in the simulations the size of the particles is fixed, but their Stokes number evolves with time according to the gas surface density at the particles location (see Eq. 1). The Stokes numbers shown in the lower-left corner in the panels are those at the particles location at 300 orbits. Since initial Stokes numbers range from about 0.01 to 30, particles are quickly trapped inside the vortex as a result of gas drag. They eventually concentrate at specific locations inside the vortex where a force balance is reached between gas drag, the centrifugal force and the star's gravity (direct and indirect terms; force balance is meant to be in the non-rotating frame centred onto the star). We find qualitatively the same trend as in [Mittal & Chiang \(2015\)](#): while particles with $St \ll 1$ and $St \gg 1$ are trapped towards the vortex centre, particles with $St \sim 1$ are shifted ahead of the vortex centre in the azimuthal direction. The orientations and relative amplitudes of the aforementioned forces implies that the force balance for $St \sim 1$ particles is reached ahead of the vortex and not behind it (see the lower-right panel in figure 3 of [Mittal & Chiang 2015](#)). We quantify the azimuthal offset of the particles with respect to the vortex by measuring the azimuth of the particles relative to the location in the vortex where the gas surface density peaks. We call it the shift angle of a particle. At 300 orbits, the largest shift angles are about 20 degrees in model g2n for $St \sim 4$, 23 degrees in model g5n for $St \sim 2$, and 13 degrees in model g10n for $St \sim 2$. Although quite significant, our maximum shift angles are smaller than in [Mittal & Chiang \(2015\)](#), who found that $St = 0.5$ particles could be shifted by as much as 45 degrees. Comparison between our models, and with [Mittal & Chiang \(2015\)](#), shows that shift angles do not depend solely on the particles Stokes number but also on the velocity differences between gas and dust, which are intimately related to the shape and strength of the vortex. We point out that the smallest shift angles are obtained in model g10n, which is the one that maximises the indirect term in the star acceleration by having the most massive, asymmetric and closest vortex. We also note a tiny shift of the particles beyond the vortex centre in the radial direction.

Since particle shift angles depend on the gas velocity

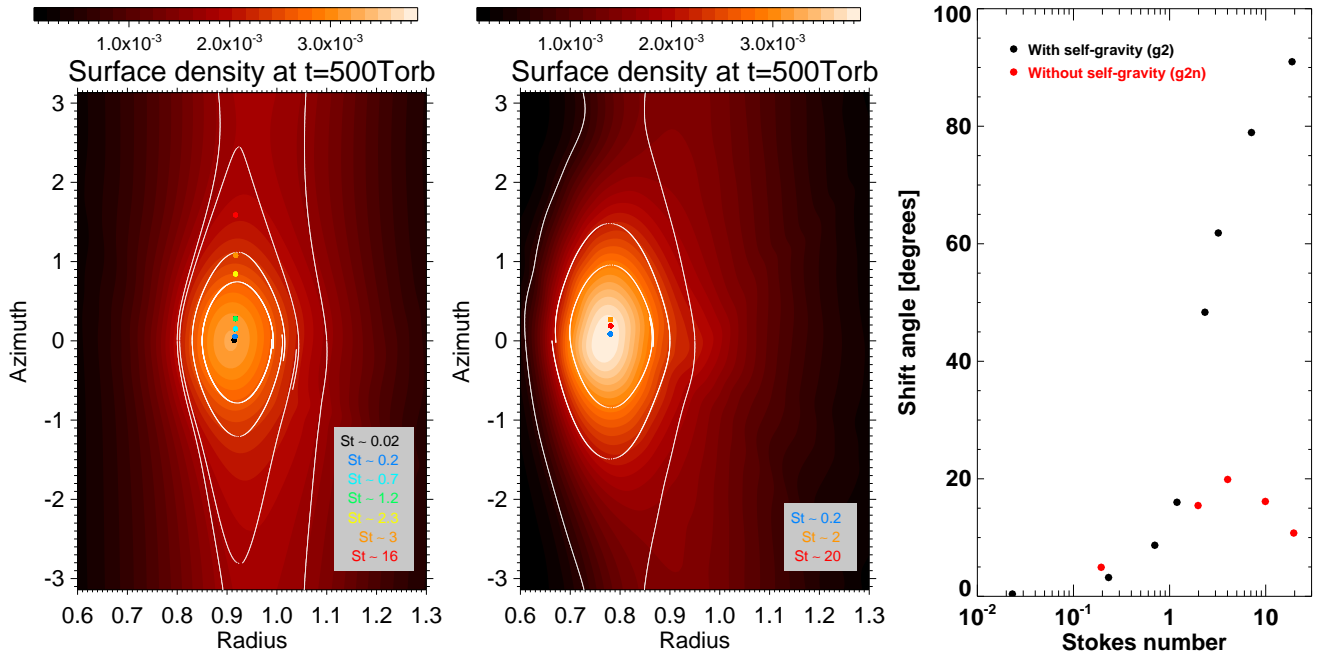


Figure 3. Results of simulations with gas self-gravity (left panel, model g2) and without (middle panel, model g2n). In both panels, contours of the gas surface density are shown in polar coordinates at 500 orbits. Streamlines in the frame rotating at the vortex’s pattern frequency are overplotted by solid white curves. The filled circles with varying colours are the instantaneous location of dust particles of various sizes. Their Stokes number at 500 orbits is indicated in the lower-right corner of the panels. The right panel displays the particles shift angle at 500 orbits as a function of their instantaneous Stokes number for models g2 (black) and g2n (red).

and density inside the vortex, they should vary as the vortex moves inward. This is illustrated in Figure 2, which displays the time evolution of the particles shift angle (left panel) and Stokes number (right panel). We see that the Stokes numbers all decrease by about 45% between 200 and 500 orbits, which is due to the increase in the gas surface density during vortex migration (the vortex migrates from $r \approx 0.72$ to $r \approx 0.55$ between 200 and 500 orbits). Variations in the particles shift angle are not as straightforward to explain. We observe that shift angles tend to decrease with time for particles with $St \lesssim 1$, and to increase with time for $St \gtrsim 2$. At the end of the simulation, $St \sim 2$ particles reach a shift angle $\gtrsim 25$ degrees, which is the largest offset that we have obtained over the duration of our simulations without self-gravity. Tests of convergence with varying grid resolution are provided in Section A of the Appendix.

As a brief summary of our results without self-gravity, we confirm the qualitative trend found by Mittal & Chiang (2015) that dust grains with Stokes number near unity are shifted azimuthally ahead of the horseshoe centre. The particles’ shift is therefore not specific to their model, where gas horseshoe streamlines result from a manually imposed circular motion of the star about the system barycentre, and can be obtained self-consistently in hydrodynamical simulations of discs unstable against the RWI.

3.2 Models with gas self-gravity

For models with self-gravity, the RWI takes longer to form a fully developed vortex than in models without self-gravity. The amplitude of the $m = 1$ mode in the Fourier analysis of the gas surface density peaks at about 40, 60 and 50 orbits for models g2, g5 and g10, respectively (it is about twice as long as in the models without self-gravity). Its stationary

value is about twice as small with self-gravity than without, illustrating that gas self-gravity hinders the RWI (Goodman & Narayan 1988).

For some of the models with self-gravity, the dust concentration is sensitive to the initial distribution of the particles, in particular whether dust is introduced before or after the vortex forms (specifically, the ring-like structures formed by the dust grains in model g5, which will be shown in Section 3.2.2, tend to be disrupted when particles are introduced before the vortex forms - they rather take the form of arc rings). However, when dust particles are introduced after the vortex reaches a quasi-steady state, their concentration shows overall marginal dependence on the initial distribution. For comparison purposes, all simulations with self-gravity have been restarted at 250 orbits (long after the vortex forms) by introducing the particles between $r = 1.2$ and 1.4 with a uniform distribution.

3.2.1 Results of model g2

The left panel of Figure 3 displays contours of the gas surface density at 500 orbits for model g2. Results are shown with polar coordinates $\{r, \varphi\}$ and the maximum in the gas surface density is set at $\varphi = 0$. For comparison, the results of model g2n (without self-gravity) are shown at the same time in the middle panel of Figure 3, using the same colour scale for the density contours (recall that, without self-gravity, particle concentration is found to be independent of the initial particle distribution). We first see that vortex inward migration is much less rapid with self-gravity, and consequently the gas surface density in the vortex is smaller with self-gravity at the same time. Actually, the vortex’s shape and strength at 500 orbits in model g2 are, overall, very similar to those of model g2n at ~ 130 orbits (not shown here). A qualitative

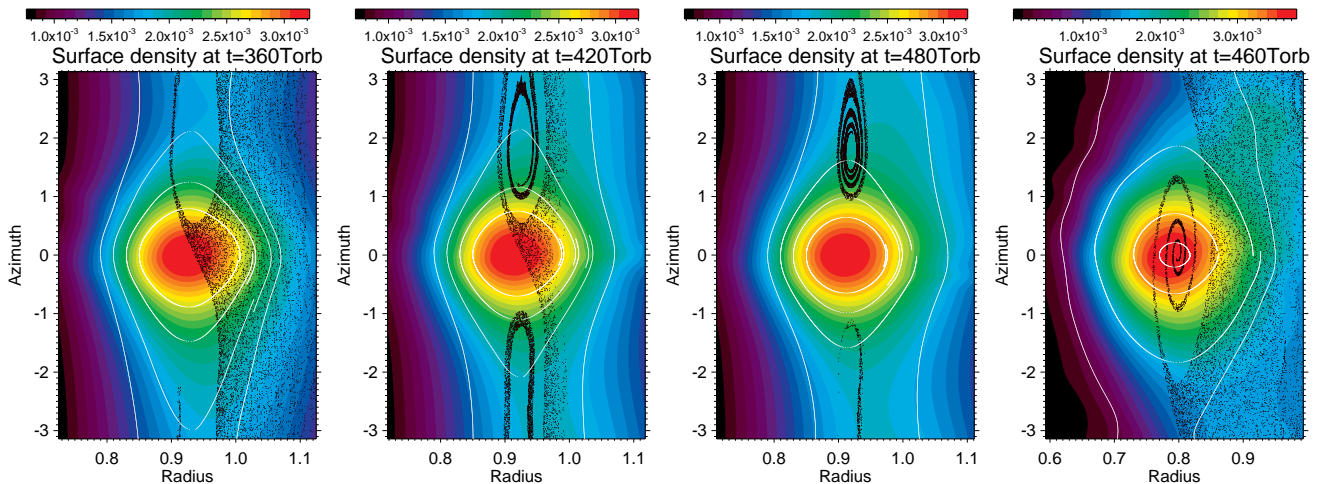


Figure 4. Results of simulations with large (typically metre-sized) particles with model g2 (three leftmost panels) and model g2n (right panel). Contours of the gas surface density are shown along with the particles location depicted by black dots, and gas streamlines overplotted by white curves. With self-gravity, large particles perform horseshoe U-turns relative to the vortex and drift much ahead of the vortex. Without self-gravity, large particles drift toward the vortex centre.

comparison of the two models at these times indicates that the density contrast in the vortex’s spiral waves is smaller with self-gravity, which is consistent with inward migration being slower in that case. A detailed interpretation for why gas self-gravity slows down the vortex’s inward migration is beyond the scope of this paper. Part of it could be due to self-gravity inhibiting the RWI and thus weakening the vortex when the disc’s surface density near the vortex’s location is large enough (Goodman & Narayan 1988, see also Paper I). It is also possible that gas self-gravity shifts the location of the vortex’s Lindblad resonances (where the flow becomes supersonic relative to the vortex). By analogy with the analytic study of Pierens & Huré (2005) for planet-disc interactions, gas self-gravity would shift Lindblad resonances outward compared to the situation where the vortex would migrate in a non self-gravitating disc. This would weaken the vortex’s outer wave, strengthen the inner wave, and explain the slowing down of the migration (with some analogy, again, with planet-disc interactions, see Baruteau & Masset 2008b).

The location of dust particles of various sizes is marked by filled circles in the left and middle panels of Figure 3, and their instantaneous Stokes number is shown in the panels. For model g2 again, dust grains quickly converge to specific locations in the disc where a force balance is reached. However, particle concentration operates differently with gas self-gravity: the particles shift angle relative to the vortex centre increases monotonically with Stokes number, ranging from ≈ 0 degrees for $St \sim 0.02$ to ≈ 90 degrees for $St \sim 16$. As shown again in the middle panel of Figure 3 for model g2n, shift angles without self-gravity increase with St up to $St \sim 1$, and decrease to zero beyond. The comparison between models g2 and g2n is further highlighted in the right panel of Figure 3, which displays the shift angle and Stokes number at 500 orbits with and without self-gravity. We stress the rapid increase of the shift angle with self-gravity when $St \gtrsim 1$. This transition occurs for particles of a few centimetres in size when using the set of physical units given as example in Section 2.3. The location where particles concentrate in model g2 is found to be independent of their initial distribution (e.g., inside or outside the vortex’s radial location),

at least for the particle sizes shown in Figure 3. Larger particles than those shown in the figure can display a different behaviour, which we describe below.

To get more insight into the behaviour of the largest particles with gas self-gravity, we show the evolution of particles 4 times larger than the largest particles displayed in Figure 3. Their physical radius is 2 metres using the set of physical units given in Section 2.3, and their initial distribution is again uniform between $r = 1.2$ and 1.4 . The time evolution of their location relative to the vortex is illustrated in the three leftmost panels in Figure 4. As particles drift in toward the vortex, they make a horseshoe U-turn ahead of the vortex centre (leftmost panel). Later, particles go on to a second U-turn (outward this time, second panel on the left). Because of gas drag, the second U-turn is closer to the vortex’s radial location, but further away in the azimuthal direction. Particles eventually drift toward their equilibrium location about 90-100 degrees ahead of the vortex (third panel). Gas streamlines, which are overplotted by white curves in the panels, recall that gas does not make horseshoe U-turns relative to the vortex. So do not the smallest particles, which concentrate towards the vortex centre. Gas streamlines also indicate that the equilibrium location of the largest particles is very close to the tip of the elliptical streamline that lies furthest from the vortex. The rightmost panel in Figure 4 shows the result of the same simulation without self-gravity, and it is clear that the large particles drift toward the vortex centre upon adopting elliptical trajectories relative to the vortex.

The horseshoe U-turns performed by large particles is most likely the consequence of the particles feeling the self-gravitating acceleration of the gas and interacting with the vortex partly as if it was a massive body. Like if it was a planet. Using the analogy with disc-planet interactions, we interpret our results based on the comparison between three timescales: (i) the timescale for dust particles to drift across the half-width of the vortex’s horseshoe region (τ_{drift}), (ii) the timescale for particles to make a U-turn relative to the vortex ($\tau_{\text{U-turn}}$), and (iii) the timescale for particles to complete a full horseshoe orbit relative to the vortex (libration timescale, $\tau_{\text{lib}} > \tau_{\text{U-turn}}$). When $\tau_{\text{drift}} \leq \tau_{\text{U-turn}}$, gas drag

prevents dust particles from making horseshoe U-turns, and dust drifts towards the vortex's centre much like when self-gravity is discarded. When $\tau_{\text{lib}} > \tau_{\text{drift}} \gtrsim \tau_{\text{U-turn}}$, dust particles can embark on, but not complete, horseshoe trajectories. Gas drag still acts to damp the relative velocity between dust and gas, and particles thus progressively concentrate at or near the vortex's radial location (as can be seen in the two middle panels in Figure 4). When $\tau_{\text{drift}} \gg \tau_{\text{lib}}$, that is when the drag force is much smaller than the effective gravitational force from the vortex, particles should undergo horseshoe orbits very similar to those a nearly inviscid gas would adopt in the presence of a planet. This is shown in the limit of fully decoupled particles ($\tau_{\text{drift}} \rightarrow \infty$) in Section B of the Appendix.

The particle Stokes number for which $\tau_{\text{drift}} \gtrsim \tau_{\text{U-turn}}$, and for which dust can embark on horseshoe U-turns relative to the vortex, can be estimated as follows. We have $\tau_{\text{drift}} = x_s/|v_{r,\text{dust}}|$ with x_s the half-width of the vortex's horseshoe region and $v_{r,\text{dust}}$ the particle radial velocity. In a 1D isothermal gas disc, and neglecting the contribution of gas self-gravity to the azimuthal velocities of the gas and dust, $v_{r,\text{dust}}$ is given by (e.g., Takeuchi & Lin 2002)

$$v_{r,\text{dust}} = \frac{1}{1 + \text{St}^2} \left(v_{r,\text{gas}} + h^2 v_K \text{St} \frac{\partial \log \Sigma}{\partial \log r} \right), \quad (2)$$

where $v_{r,\text{gas}}$ is the radial velocity of the gas and v_K is the Keplerian velocity. All quantities in Eq. (2) should be evaluated at the separatrices of the vortex's horseshoe region (that is, at $r = r_v \pm x_s$, with r_v the vortex's radial location). Progress can be made by considering the 2D structure of the vortex. For model g2, our numerical simulations show that $v_{r,\text{gas}}$ is fairly well approximated by

$$v_{r,\text{gas}} = -\frac{5h^2}{2} v_K \frac{\partial \log \Sigma}{\partial \varphi}, \quad (3)$$

which is actually 5 times the first-order correction for the gas radial velocity to maintain a geostrophic flow about the vortex (balance between Coriolis and pressure forces; see, e.g., equation 16 in Mittal & Chiang 2015). The difference accounts for the zero-order radial velocity of the gas. We then find that $v_{r,\text{gas}}(r = r_v \pm x_s) \approx \pm h^2 v_K$, with $v_{r,\text{gas}}(r = r_v - x_s)$ evaluated behind the vortex in the azimuthal direction (where outward U-turns occur), and similarly $v_{r,\text{gas}}(r = r_v + x_s)$ is evaluated ahead of the vortex in the azimuthal direction (where inward U-turns occur). The radial density profile of the gas being weakly altered by the vortex's formation, the last term in the bracket in Eq. (2) can be calculated with the initial surface density profile, which gives $\partial \log \Sigma / \partial \log r(r = r_v \pm x_s) = \mp r_v x_s / 4H^2$. Eq. (2) can finally be recast as

$$v_{r,\text{dust}}(r = r_v \pm x_s) = \frac{v_K}{1 + \text{St}^2} \left(\pm h^2 \mp \frac{\text{St} x_s}{4 r_v} \right). \quad (4)$$

We first note that, for dust horseshoe U-turns to be possible, we need $v_{r,\text{dust}}(r = r_v - x_s) > 0$ (outward U-turn) and $v_{r,\text{dust}}(r = r_v + x_s) < 0$ (inward U-turn), which implies $\text{St} > 4h^2 r_v / x_s$. For the vortex in model g2, $x_s / r_v \approx 0.04$ and above inequality becomes $\text{St} \gtrsim 1$. From our numerical simulations, we find $\tau_{\text{U-turn}} \sim (2 - 3) \times T_{\text{orb}}$ which, as expected, is a small fraction of τ_{lib} ($\tau_{\text{lib}} = 8\pi r_v / 3\Omega x_s \approx 35T_{\text{orb}}$). Using Eq. (4), we finally find that $\tau_{\text{drift}} \gtrsim \tau_{\text{U-turn}}$ for $\text{St} \gtrsim 2 - 4$. It is in good agreement with the range of Stokes numbers from which gas self-gravity considerably increases the particle shift angle in model g2 (see right panel of Figure 3).

For completeness, we mention that the same self-gravitating simulation as shown in the three leftmost panels in Figure 4, but where particles are placed initially between $r = 0.5$ and 0.7 , result in the particles concentrating both ahead (at ~ 100 degrees) and behind (at ~ -100 degrees) the vortex centre. This shows that the concentration of the largest particles, either far ahead or far behind the vortex, depends on the relative flow between the dust and the vortex, that is on the initial location of the particles (inside or outside the vortex's radial location), as well as the direction of vortex migration (not shown here). We point out again the analogy with disc-planet interactions, where gas drifting relative to a low-mass planet – because the planet migrates and/or the gas drifts viscously – can be trapped ahead or behind the planet (Masset 2002; Paardekooper 2014; Pierens 2015). We also stress the analogy with the trapping of solid particles on tadpole orbits around a planet in the presence of gas drag (e.g., Peale 1993; Lyra et al. 2009). The equilibrium location of solid particles ahead or behind the planet depends on the planet's mass and on the particle size, and, interestingly, the maximum shift angle of solid particles ahead of a planet is 108 degrees (Peale 1993), which is very close to the maximum shift angle that we find for a self-gravitating vortex.

As a brief summary of our results for model g2, we find that gas self-gravity controls the dynamics of large particles, whereas gas drag determines the dynamics of small particles. Self-gravity allows the largest particles to concentrate far ahead of the vortex (or far behind it) upon adopting horseshoe U-turns. Gas drag prevents small particles from taking the U-turns. The transition between what could be called a gas drag-dominated regime and a self-gravity-dominated regime occurs quite neatly around $\text{St} \approx 1$ for model g2. However, the Stokes number at this transition likely depends on the disc mass. For example, in a disc with lower gas surface density near the vortex's radial location, the magnitude of the drag force will be approximately the same for a given Stokes number (approximately since the vortex's shape and strength may vary with the disc's surface density), but the gravitational force from the vortex will be smaller since the vortex is less massive. Results of simulations at lower gas surface densities will be presented at the beginning of Section 4, which indicate that the transition between the gas drag and self-gravity dominated regimes occurs around a critical particle size.

3.2.2 Results of model g5

The results of model g5 are displayed in Figure 5 at 500 orbits. We see that both the gas structure and the dust distribution are markedly different from those of model g2, while the initial gas densities differ by only a factor of 2.5 between both models (compare with the left panel of Figure 3). In model g5, the vortex is more elongated along the azimuthal direction and the density contrast is about 20%. For comparison, in model g2 the density contrast along the vortex is by a factor of ~ 2 . Furthermore, in model g5 the gas density maximum in the vortex is still very close to $r = 1$, indicating that the vortex has not migrated over the duration of the simulation. This is supported by a detailed inspection at the gas density which shows marginal excitation of density waves by the vortex compared to model g2. Also, we notice that the radial location where elliptical streamlines are centred in the

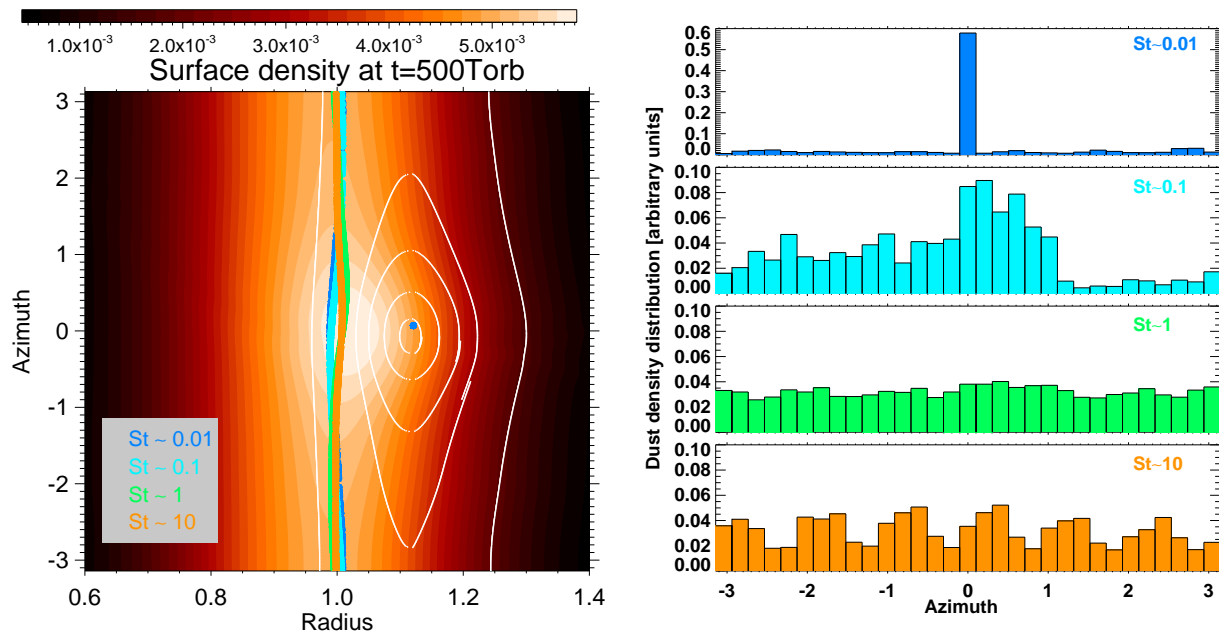


Figure 5. Results of model g5 at 500 orbits. Left: contours of the gas surface density with gas streamlines relative to the vortex (white curves) and particles location (filled circles). Right: instantaneous dust density distribution with azimuth (see text). The colours used for the particles are the same in both panels, and the space-averaged Stokes number of the particles is indicated in the panels.

frame rotating at the vortex’s pattern frequency, which defines the vortex’s corotation radius, is shifted outward from the vortex’s radial location (defined as the radial location where the gas surface density peaks). This shows that the vortex’s pattern frequency is slower than the Keplerian frequency (Paper I). This slow pattern frequency is probably the reason why the vortex emits no or very little spiral density waves in the disc. The slow pattern frequency also directly impacts the particles distribution. Most of the small particles get trapped onto the elliptical streamlines in the rotating frame and progressively drift toward the centre of the set of elliptical streamlines (which actually corresponds to a minimum in the gas potential vorticity or vortensity). This is what we obtain for the $St \sim 0.01$ particles (see the single blue dot at $r \approx 1.12$ in the left panel of Figure 5). Note, however, that some of the $St \sim 0.01$ particles form a ring-like structure around the vortex’s radial location at $r \approx 1$.

Larger particles decouple from the gas and are not tied to the elliptical streamlines: they converge toward the pressure maximum located at $r \approx 1$. They also form ring-like structures, though the left panel in Figure 5 does not hint at the particles azimuthal distribution. The latter is shown as an histogram in the right panel of Figure 5, with large bins used to smooth high spatial frequency fluctuations (the y-values in the histogram are simply the fraction of the total number of particles in each bin). Azimuths are relative to the vortex centre. More than half of the smallest ($St \sim 0.01$) particles are at $\varphi \sim 0$, with the vast majority of them at the centre of the elliptical streamlines. Larger particles show quite distinct azimuthal distributions. $St \sim 0.1$ particles have a lopsided distribution that peaks slightly ahead of the vortex. The fact it peaks ahead of the vortex is just a coincidence: since $St \sim 0.1$ particles and the vortex move at different speeds, the azimuth at which the particles’ azimuthal distribution peaks varies with time. Finally, while $St \sim 1$ particles have a nearly flat azimuthal distribution,

$St \sim 10$ particles feature a periodic pattern of azimuthal wavenumber $m = 6$. The reason for this particular pattern is unknown, but resembles that of the $St \sim 0.01$ particles located around the vortex’s radial location. We find the same pattern when adopting a slightly different initial distribution (uniform in $r \in [0.8 - 1.2]$). We also comment that the vortex’s corotation radius becomes less shifted as grid resolution is increased. It is located at $r \approx 1.05$ for a grid resolution increased to 600×1000 , compared to $r \approx 1.12$ for our nominal resolution of 300×600 . More detailed tests of convergence in resolution with self-gravity are presented for model g10 in Section 3.2.3.

To get more insight into the different gas and dust behaviours between models g2 and g5, we have restarted the simulation with model g5 at 350 orbits by imposing a slow decrease in the radial profile of the gas surface density. By doing this we expect to see a smooth transition in the concentration of the large dust grains from ring-like structures (as in model g5) to point-like structures (as in model g2). Specifically, as in Baruteau & Papaloizou (2013) we adopt a simple exponential decay of the density profile by solving $\partial_t \Sigma = -(\bar{\Sigma} - \Sigma_{\text{target}})/\tau$ alongside the hydrodynamical equations, with $\bar{\Sigma}$ the azimuthally-averaged density profile at restart time, $\Sigma_{\text{target}} = 10^{-3}\bar{\Sigma}$ an arbitrarily small density profile that we take to be not zero for numerical convenience, and τ is chosen to be 300 orbits. In practice, the axisymmetric profile of gas density is decreased by a factor ~ 10 in about 700 orbits after the restart. The results of this simulation are displayed at four different times in Figure 6, where the Stokes numbers shown in the panel are averaged in space (they increase with time as the gas surface density decreases). The first panel from the left is at 700 orbits (350 orbits after the restart). Interestingly, the gas density profile now takes smaller values than in model g2, yet both the gas and the dust distributions are very similar to those of model g5 prior to the restart. We note a few differences, though. First, the centre of the gas elliptical streamlines in the rotat-

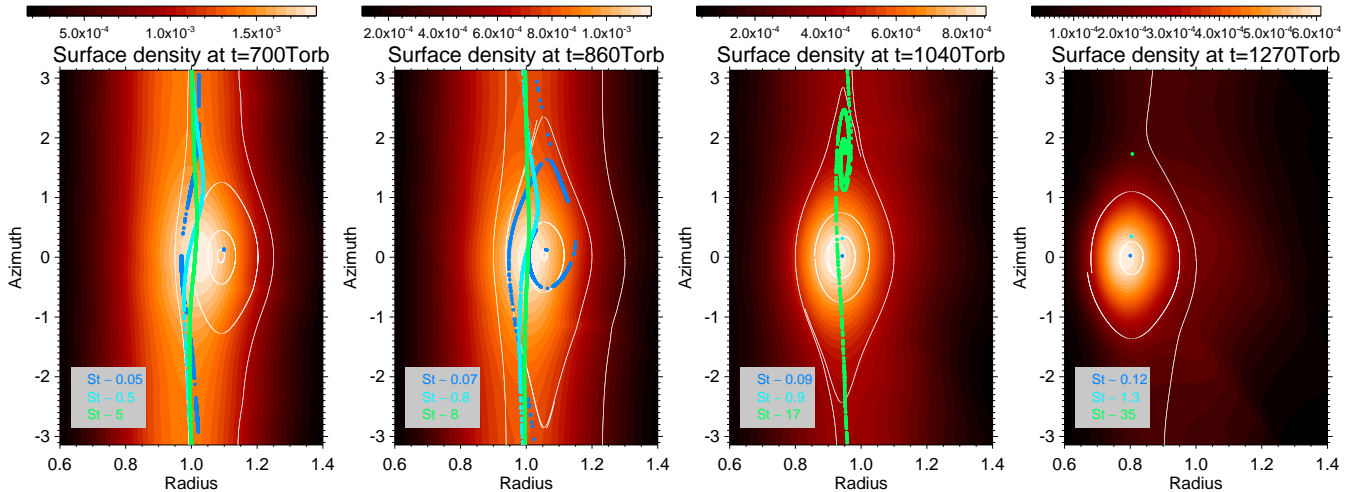


Figure 6. Results of the restart simulation with model g5 where a slow decrease in the radial profile of the gas surface density is imposed (see text). As in previous figures, all panels show contours of the gas surface density with gas streamlines in the frame rotating at the vortex’s pattern frequency (white curves) and the location of particles of different sizes (filled circles). The averaged Stokes number of the particles is shown in the lower-right corner in the panels.

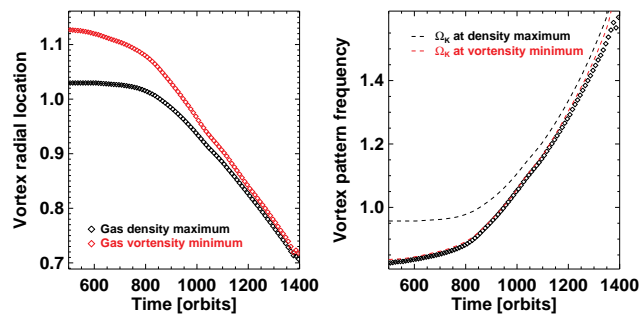


Figure 7. Results of the restart simulation with model g5 where a slow decrease in the radial profile of gas surface density is imposed. Left: time evolution of the radial location where the gas surface density peaks in the vortex (black symbols), and where the gas potential vorticity is minimum, which is the centre of the elliptical streamlines in the rotating frame (red symbols). Both locations coincide when the local disc mass becomes small enough. Right: vortex’s pattern frequency (black symbols) and Keplerian frequency at both previous locations (dashed curves).

ing frame is slightly closer to the vortex’s centre (its radial location has decreased from $r \approx 1.12$ to $r \approx 1.08$). Second and probably related point, the smallest particles that are located around the vortex’s radial location now form a disrupted ring (see the dark-blue dots in the panel). In the second panel (at 860 orbits), the centre of the elliptical streamlines has become close enough to the vortex centre to significantly perturb the smallest particles, which become trapped onto elliptical streamlines. In the third panel (1040 orbits), the centre of the elliptical streamlines now coincides with the vortex centre, which indicates that the vortex’s pattern frequency is now very close to the Keplerian frequency. In addition, the vortex is now less elongated along the azimuthal direction (the density contrast along the vortex increases) and it has started to migrate inward (the vortex’s radial location has decreased from $r \approx 1$ to ≈ 0.92 from 860 to 1040 orbits). Particles with the two smallest sizes now have point-like distributions (dark-blue and cyan dots

in the panel), while the largest particles are getting trapped much ahead of the vortex. In the fourth panel (1270 orbits) particles have point-like distributions which are very close to those shown in Figure 3 for model g2.

Before closing this subsection, we come back to the evolution of the vortex’s pattern frequency with gas self-gravity. We have seen that, with increasing strength of self-gravity, the radial location where the gas potential vorticity is minimum (the vortex’s corotation radius) shifts outward from the radial location where the gas density peaks (which we have defined throughout this study as the vortex’s radial location). This is further illustrated and quantified in the left panel of Figure 7 for the restart simulation with model g5 where the gas density decreases over time. We have calculated the vortex’s pattern frequency by measuring the angle through which the density maximum rotates over time (it is the same angle as that through which the minimum potential vorticity rotates over time). The time evolution of the vortex’s pattern frequency is displayed in the right panel of Figure 7. Dashed curves show the Keplerian frequency at the radial location where the gas density is maximum (in black) and where the potential vorticity (vortensity) is maximum (in red). The vortex’s pattern frequency nearly equals the Keplerian frequency at the radial location of the vortensity minimum, as expected, and catches up with the Keplerian frequency at the density maximum as the strength of self-gravity decreases.

3.2.3 Results of model g10

The results of model g10 are displayed in Figure 8 at 500 orbits. Overall, the gas and dust distributions are similar to those of model g5 at the same time (compare with Figure 5). The smallest particles also tend to concentrate at the centre of the elliptical streamlines located at the vortex’s corotation radius. The latter is shifted further outside the vortex’s radial location compared to model g5 (the vortex’s corotation radius is at $r \approx 1.2$ for model g10 and at $r \approx 1.12$ for model g5). This goes along the trend illustrated at the end of the previous subsection that the larger the

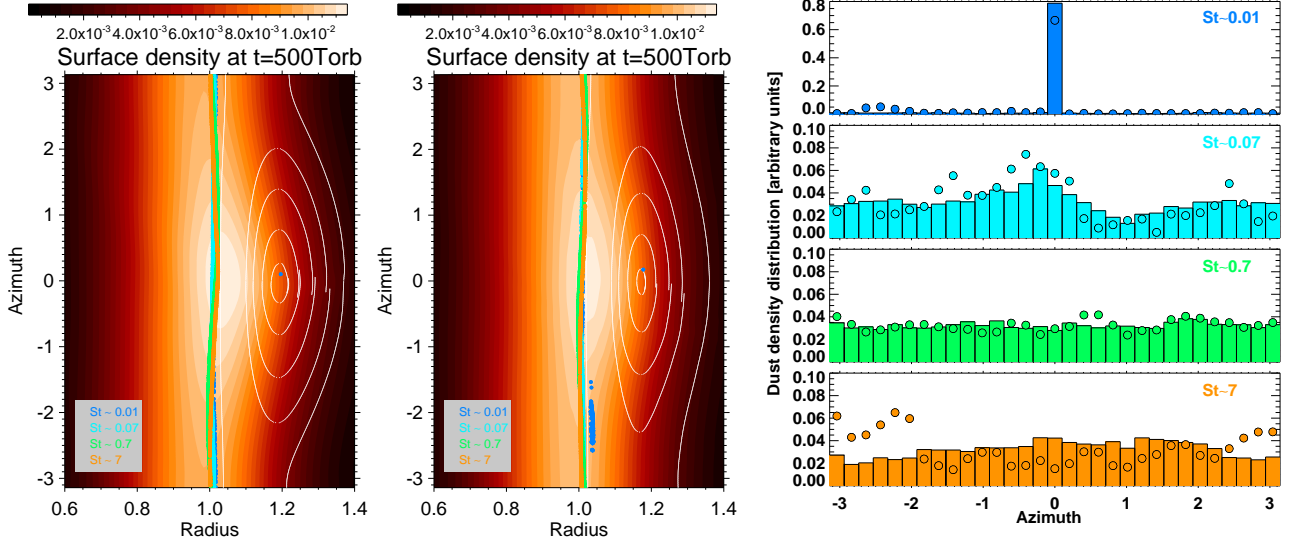


Figure 8. Results of model g10 at 500 orbits with our fiducial grid resolution (300×600 , left panel) and at higher resolution (600×1000 , middle panel). Left and middle panels: contours of the gas surface density with gas streamlines relative to the vortex (white curves) and particles location (filled circles). Right: instantaneous dust density distribution versus azimuth, with histogram bars for the run at nominal resolution and filled circles for the run at high resolution. The colours used for the particles are the same in the three panels, and the space-averaged Stokes number of the particles is indicated in the panels.

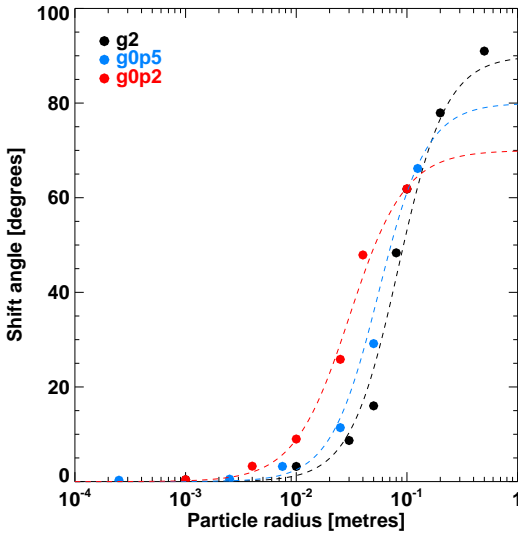


Figure 9. Shift angle relative to the vortex centre for various particle sizes in models g2, g0p5 and g0p2. Dashed curves are simple fitting functions (see text).

disc mass (that is, the stronger self-gravity), the slower is the vortex's pattern frequency compared to the Keplerian frequency. Larger particles concentrate along rings with different azimuthal structures depending on the particle size (and thus Stokes number). Figure 8 also displays the results of model g10 with a grid resolution increased from 300×600 to 600×1000 (middle panel, filled circles in the right panel). Results at both resolutions are in fairly good agreement. The vortex's corotation radius decreases from $r \approx 1.2$ at a resolution of 300×600 to $r \approx 1.18$ at a resolution of 600×1000 . Convergence in resolution is much better than for model g5, which suggests that the transition to the regime where self-gravity renders the vortex's pattern frequency sub-Keplerian is very sensitive to grid resolution.

4 SYNTHETIC DUST CONTINUUM OBSERVATIONS

In this section, we use the dust distribution in our simulations of self-gravitating lopsided discs to produce synthetic images of dust continuum observations. We focus on the models where the gas surface density at the vortex location is lower or equal than in model g2, for which, using the physical units of Section 2.3, grains up to few centimetres in size have nearly stationary point-like distributions around the vortex's radial location. (In contrast, in models with larger gas densities like models g5 and g10, grains larger than about 1 cm have non-axisymmetric ring-like distributions with non-trivial dependence on grain size, and are non-stationary in a frame rotating at the vortex's frequency, which makes it more delicate to predict the corresponding dust continuum emission). Particle shift angles relative to the vortex centre are displayed in Figure 9 for models g0p2, g0p5 and g2 at 500 orbits after the beginning of the simulations (250 orbits after introduction of the particles). For each model, particles larger than the largest size shown in the figure describe ring-like structures centred around the vortex's radial location.

To translate the dust distribution in our simulations into dust surface density, we assume that dust grains have a size distribution $n(s) \propto s^{-p}$ from $30 \mu\text{m}$ to 20 cm . The value of p is very uncertain, especially in the context of dust trapping in a vortex, and we allow it to vary from 3 to 2.5. We divide the above size range into small size bins with a logarithmic spacing. We assume that grains smaller than 0.5 mm follow the gas distribution, and that larger grains have point-like distributions shifted ahead of the vortex. Particles are assigned shift angles ($\delta\varphi$) through fits of the results of simulations shown in Figure 9. For model g2, we find good agreement with $\delta\varphi(s) = 90^\circ \times 0.5 \{1 + \tanh(2.6 \log_{10}(14s))\}$ with s in metres (see the black dashed curve in Figure 9). For model g0p5, we use $\delta\varphi(s) = 80^\circ \times 0.5 \{1 + \tanh(2.3 \log_{10}(18s))\}$ (blue dashed curve in the figure), and for model g0p2,

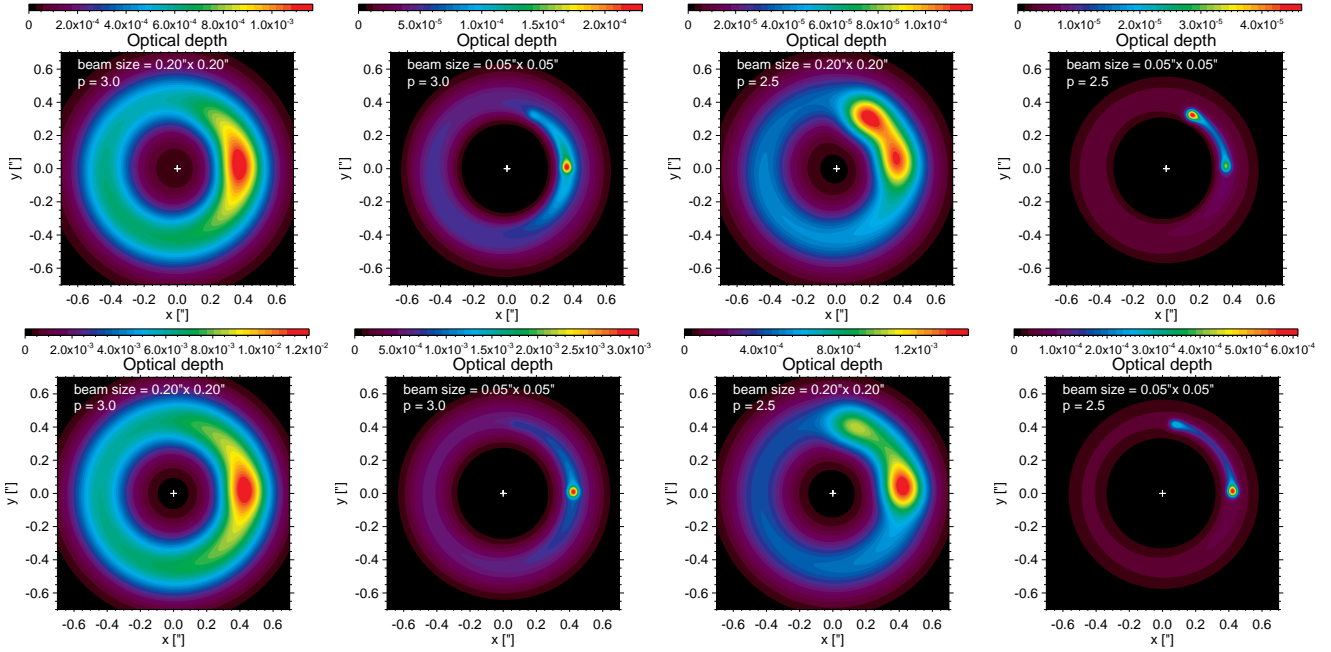


Figure 10. Synthetic images at 37.5 GHz (8 mm) of the disc’s optical depth obtained from our simulations with models g0p2 (upper panels) and g2 (lower panels). The value of p (minus the power-law index of the grains size distribution) equals 3 in the two columns on the left-hand side, and 2.5 on the right-hand side. Convolution is done with a Gaussian beam size of FWHM set to $0.2''$ or $0.05''$. The plus sign at the origin marks the star’s location.

$\delta\varphi(s) = 70^\circ \times 0.5 \{1 + \tanh(2 \log_{10}(33s))\}$ (red dashed curve). The dust’s surface density in each size bin is then derived assuming a total dust-to-gas mass ratio of 1%, and converting our results of simulations into physical units using the set of units in Section 2.3.

We use Mie theory to determine the dust opacity in each size bin at a wavelength of 8 mm (37.5 GHz). See [Zhu & Stone \(2014\)](#) for more details (their section 4.3). The dust opacities per unit dust mass at 8 mm are 1.2×10^{-3} , 1.7×10^{-3} , 1.4×10^{-2} , 0.79, 0.67, 0.15, 5.2×10^{-2} and 1.0×10^{-2} $\text{cm}^2 \text{g}^{-1}$ for grains of radius 30 μm , 100 μm , 300 μm , 1 mm, 3 mm, 1 cm, 3 cm and 20 cm. We finally multiply the dust’s surface density in each size bin with the interpolated opacity and add these products together to get the disc’s optical depth. Synthetic images are produced by convolving the disc’s optical depth with a Gaussian kernel of FWHM equal to $0.05''$ or $0.2''$. The disc is assumed to be located at 140 parsecs and to be seen face-on.

Synthetic images are displayed in Figure 10 for models g0p2 (upper panels) and g2 (lower panels). Values of p (minus the power-law index of the dust size distribution), and of the FWHM of the Gaussian kernel by which the total optical depth is convolved, are indicated in the top-left corner in the panels. These images show that, for steep size distributions ($p \geq 3$), the dust continuum emission at 8 mm displays a lopsided distribution with a peak emission at the vortex centre (where the gas surface density is maximum). For shallower size distributions ($p \lesssim 2.5 - 3$), however, the dust continuum emission at 8 mm features a double-peaked distribution, with one peak at the vortex centre, and a second peak shifted ahead of the vortex centre in the azimuthal direction, which corresponds to the emission of grains of a few centimetres in size. The azimuthal shift of the second peak depends on the azimuthally-averaged surface density of the gas at the vortex’s radial location, $\langle \Sigma_V \rangle$ (Figure 9). It

is about 70 degrees in model g0p2, where $\langle \Sigma_V \rangle \approx 0.5 \text{ g cm}^{-2}$ at $\approx 50 \text{ AU}$, and goes up to nearly 90 degrees in model g2, where $\langle \Sigma_V \rangle \approx 5 \text{ g cm}^{-2}$ at $\approx 60 \text{ AU}$.

Such double peak continuum emissions, if observed at mm/cm wavelengths like with ALMA or the VLA, could reveal the size segregation due to gas self-gravity between small and large dust grains trapped in a crescent-shaped vortex. There is so far no clear evidence for double peak emissions similar to what our dusty horseshoe model predicts. The double peak emission observed with ALMA in the HD 142527 disc is most probably caused by shadows cast by the tilted inner disc over the lopsided outer disc ([Casasus et al. 2015b](#); [Marino et al. 2015b](#)). VLA (0.9 cm) and ALMA Band 7 (0.8 mm) continuum emissions of the MWC 758 disc show two intensity peaks located to the north-west and to the south of the star ([Marino et al. 2015a](#)). These authors show that two dust-trapping vortices could account for the double peak continuum emissions, and the fact the VLA emission is more compact than the ALMA emission. In their model, the vortex to the south would be slightly closer to the star (at $\sim 90 \text{ AU}$) than the one to the north-west (at $\sim 120 \text{ AU}$). It would be interesting to check whether our dusty horseshoe model, which comprises a single vortex, could also reproduce the double peak distribution in the MWC 758 disc. The large-scale spirals observed in near-IR ([Benisty et al. 2015](#)) could greatly complicate the dust concentration properties, whatever the number of dust-trapping vortices to reproduce the double peak continuum emission at mm/cm wavelengths. We also stress that in the synthetic sub-mm images of [Regály et al. \(2012\)](#), a single elongated vortex in the gas disc can produce either one or two peaks of emission due to beam dilution effects (especially when angular resolution is moderate and the beam is highly elongated; Zs. Regály, priv. comm.).

5 CONCLUDING REMARKS

We examine in this paper the concentration properties of large dust grains in protoplanetary transition discs characterised by a lopsided crescent-shaped distribution in the gas surface density. 2D hydrodynamical simulations have been carried out including both gas and dust, with dust modelled as test particles undergoing gas drag (Epstein regime). The lopsided distribution in the gas is obtained by adopting a ring-like gas density profile that becomes unstable against the Rossby-wave instability. The instability saturates into a large-scale vortex that efficiently traps the grains. This trapping mechanism is often invoked to interpret the crescent-shaped continuum emission imaged by sub-millimetre interferometers in some transition discs (e.g., Regály et al. 2012).

In accompanying Paper I (Zhu & Baruteau, submitted) we explore the role of gas self-gravity and of the disc mass in shaping the vortex structure. Their impact on the trapping of dust grains is the scope of the present paper. We first present results of models without gas self-gravity, for which we find that the indirect force resulting from the displacement of the star by the vortex plays a prominent role in the gas and dust dynamics, in agreement with Mittal & Chiang (2015). While grains with Stokes number (stopping time to orbital time ratio, St) much smaller and much larger than unity are trapped near the vortex centre, particles with $St \sim 1$ are shifted ahead of the vortex in the azimuthal direction. This is in good qualitative agreement with the results of test particle integrations by Mittal & Chiang (2015). We find particle shift angles relative to the vortex centre that go up to 20–25 degrees for $St \sim 2 - 4$ particles, depending on the disc mass, which strongly affects the shape and orbital evolution of the vortex. Our maximum shift angles are a factor ~ 2 smaller than in Mittal & Chiang (2015).

We then present results with gas self-gravity, and find that it largely affects dust trapping in the vortex. At low to moderate gas surface densities at the vortex’s radial location (local Toomre parameter $\gtrsim 10$), we find gas self-gravity to be most important for large grains. Grains with $St \lesssim 1$ (typically smaller than 1 cm) have similar shift angles with and without self-gravity, as gas drag plays a major role in determining the dynamics of small particles. The dynamics of larger particles ($St \gtrsim 1$) becomes increasingly dominated by gas self-gravity, and we find that shift angles increase very rapidly with increasing grain size (Figure 9). We find shift angles of about 50 degrees for grains of 3–5 cm in size, and up to 90 degrees for ~ 10 cm grains. We show that these large shift angles result from the large particles undergoing horseshoe U-turns relative to the vortex before drifting to their equilibrium location via gas drag. The horseshoe U-turns arise because of the self-gravitating acceleration of the gas exerted on the particles, which therefore interact with the vortex as if it was a massive body. The limit case of fully decoupled particles actually shares a number of analogies with the evolution of inviscid gas near a low-mass planet. Synthetic images produced from our simulations show that the size segregation caused by self-gravity between the smallest and largest grains at the vortex’s radial location could cause a double peak in the dust’s continuum emission, depending on the dust’s size distribution. The same size segregation, which does not mix the smallest and largest grains at the vortex centre, could have interesting consequences on core growth inside the vortex, and on dust feedback onto the gas.

At large gas surface densities at the vortex’s radial lo-

cation (local Toomre parameter $\lesssim 10$), self-gravity renders the vortex’s pattern frequency slower than the Keplerian frequency. This shifts the vortex’s corotation radius outside the radial location where the lopsided gas density distribution is maximum. Consequently, (most of) the smallest particles concentrate in point-like distributions that are shifted slightly outside the gas density maximum. Conversely, larger particles ($St \gtrsim 0.1$) describe ring-like structures, some of them lopsided, which are centred about the radial location where the gas density peaks (Figures 5 and 8).

Our study highlights that the concentration of large dust grains is sensitive to the shape of the vortex, which depends on the gas model. The main result of Paper I is that self-gravity plays a prominent role in structuring the vortex in massive discs. The main result of the present paper is that self-gravity plays a prominent role in setting particle concentration within the vortex even at low disc masses.

There are several ways that the physical model used in this work can be improved. Inclusion of an energy equation for the gas, of the disc’s vertical stratification (via 3D simulations), and of possibly important feedback effects of dust concentration onto the gas are some of them. Another outstanding question is that of the particles concentration in a vortex formed at the outer edge of a gap-opening planet, which could be significantly impacted by the planet wakes. More generally, a pressing, yet unsolved issue is that of the excitation and long-term maintenance of a large-scale vortex through the RWI. In this work, we have assumed a narrow ring-like density profile for the (nearly inviscid) gas plus an ad hoc $m = 1$ seed perturbation; however, there is no robust way to generate either. Non-axisymmetric seed perturbations could be induced by disc turbulence, embedded planet companions or nearby stars. Several mechanisms mentioned in the third-to-last paragraph in the introduction could provide the necessary axisymmetric density (vortensity) extremum, like for instance an effective viscosity jump at the transition between magnetically active and inactive regions. But, again, more work is needed to assess whether these mechanisms, and the vortices that they trigger, have a long lifetime.

APPENDIX A: CONVERGENCE WITH GRID RESOLUTION

We have carried out tests of convergence with increasing grid resolution for the non self-gravitating models g2n and g5n. Each model was simulated with the same particle size, and with the number of grid cells in the radial times azimuthal directions increased from 200×400 to 500×1000 for model g2n, and up to 600×1200 for model g5n. Results are displayed in Figure A1. For model g2n (upper panels) convergence in resolution is fairly good, with the particles shift angle and Stokes number varying by less than 10% between our nominal resolution (300×600) and maximum resolution. This fairly good convergence is not surprising since our gas model aims at producing a large-scale lopsided distribution in the gas surface density ($m = 1$ mode). Convergence is not excellent either. It is due to the fact that vortex inward migration occurs at a pace that slightly increases with increasing resolution. Visual inspection at the gas density at different resolutions points to a larger density contrast of the vortex waves with increasing resolution, which relates to a larger angular momentum flux extracted

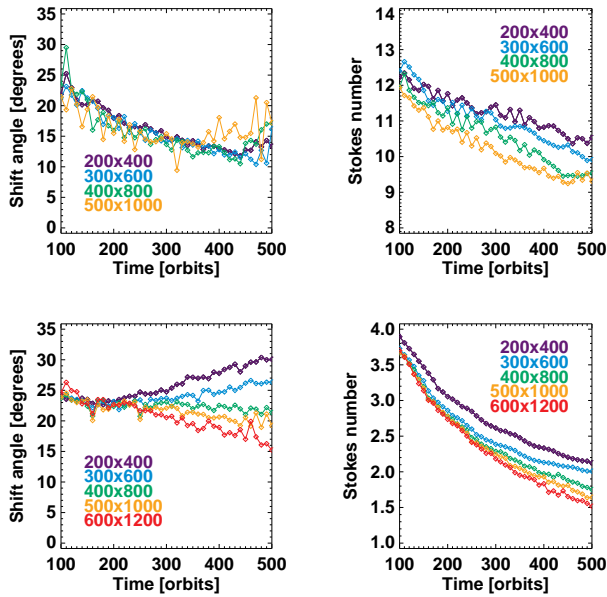


Figure A1. Time evolution of the particles shift angle and Stokes number in models g2n (upper panels) and g5n (lower panels) when varying the grid resolution. The grid resolution is shown in the panels as $N_r \times N_s$ with N_r and N_s the number of grid cells in the radial and azimuthal directions, respectively.

from the vortex and carried away by the waves, and therefore faster inward migration (note again the analogy with planetary migration). Increasing resolution therefore tends to strengthen the vortex and increase the gas density inside the vortex, which causes the particles Stokes number to slightly decrease, explaining our results. This behaviour is also apparent in model g5n up to about 300 orbits, after which discrepancies with varying resolution are found to increase, due to the proximity of the vortex to the inner edge of the computational domain and the resulting partial reflection of waves at that location. Apart from when the vortex gets too close to the grid's inner edge, convergence with grid resolution is satisfactory and our results show that the moderate grid resolution adopted throughout this work is sufficient for our purposes. Tests of convergence in resolution with self-gravity are presented for model g10 in Section 3.2.3.

APPENDIX B: SELF-GRAVITATING SIMULATIONS WITH DECOUPLED DUST PARTICLES

We have shown in Section 3.2 that with gas self-gravity and moderate disc mass (model g2), the larger the particles, the further they concentrate ahead of the vortex. We have shown this behaviour to be related to horseshoe U-turns performed by the large particles relative to the vortex before they drift to their equilibrium location through gas drag. In this section, we report the results of a simulation with model g2 and fully decoupled dust particles. At 250 orbits, we restarted the simulation by introducing 100 000 particles with a sharply decreasing radial distribution in $r \in [0.9 - 1]$. Results are displayed in Figure B1 at 21 orbits after the restart (upper panels) and 527 orbits after (lower panels). While the left

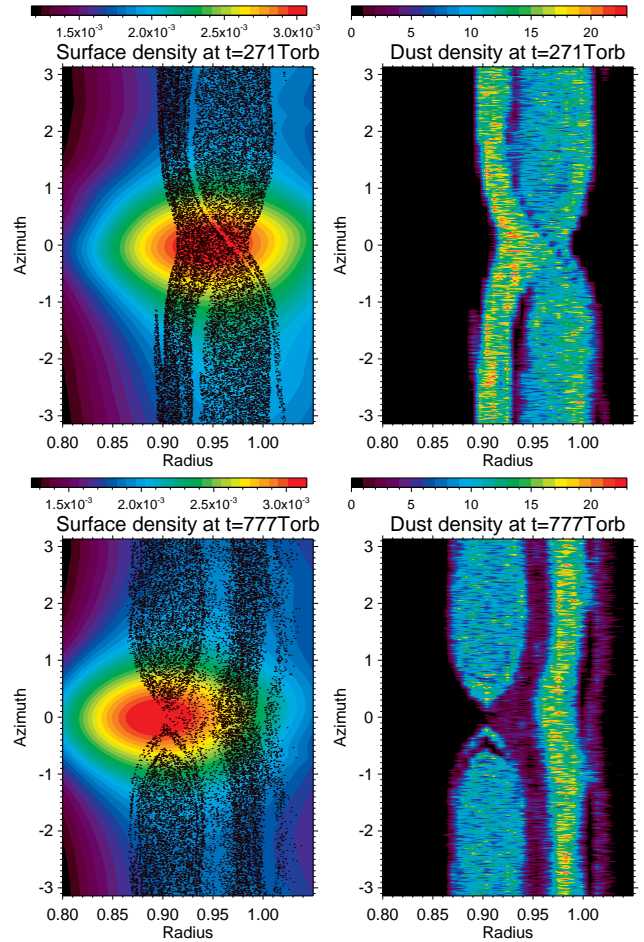


Figure B1. Results of model g2 with dust particles fully decoupled from the gas. Contours of the gas surface density with the particles location overplotted by black dots are shown in the left panels. The dust density distribution is displayed in the right panels (see text). Results are shown at 271 and 777 orbits in the upper and lower panels, respectively.

panels help locate the particles relative to the vortex, the right panels display the dust's density distribution, which we simply calculate as the number of particles per grid cell. The upper-right panel is strongly suggestive that the particles number density is advected inside what already appears as the vortex's horseshoe region. In comparison, in the lower panels the vortex has slightly migrated inward, with two notable consequences: (i) the dust density is nearly uniform in the distinct horseshoe region of the vortex, and (ii) the region of highest dust density, which is initially inside the vortex's orbit, ends up circulating relative to the vortex beyond its horseshoe region. These results are analogous to the advection of gas potential vorticity and/or entropy in the presence of a low-mass planet (e.g., Baruteau et al. 2014).

In the lower panels of Figure B1, the full width of the vortex's horseshoe region is ≈ 0.07 . Although the vortex is not a point mass, it is instructive to compare its horseshoe width to that expected for a planet with the same mass. We estimate the mass of the vortex (m_v) as the mass between $r = 0.84$ and $r = 0.95$, $\varphi = \pm\pi/4$, and having uniform surface density $\approx 3 \times 10^{-3}$ in code units (see lower-left panel in Figure B1). We obtain $m_v \approx 4.6 \times 10^{-4} M_*$. In the circular restricted three-body problem, the maximum full width of

the horseshoe region of a planet with mass m_v and orbital distance r_v is $2\sqrt{12} \times r_v(m_v/3M_\star)^{1/3}$ (Murray & Dermott 1999), which amounts here to ≈ 0.33 . Using three-body integrations, we find that the maximum full width for test particles to undergo periodic horseshoe trajectories with a small epicyclic motion is ≈ 0.10 , which is about twice the planet's Hill radius $(2r_v(m_v/3M_\star)^{1/3})$. Finally, the maximum full width of the planet's horseshoe region in the gas with same aspect ratio ($h = 0.1$) and same viscosity as in the simulations presented throughout this study is ≈ 0.14 . Not surprisingly, the width of the vortex's horseshoe region is smaller than all above estimates for a planet with the same mass as the vortex's. We note that, since $m_v/M_\star \lesssim h^3$, the planet's horseshoe width in the gas scales as $\sqrt{m_v}$ (e.g., Masset et al. 2006), which indicates that the vortex's horseshoe width in the simulation shown in Figure B1 is very similar to that of the gas around a planet of mass $m_v/4 \approx 10^{-4}M_\star$.

ACKNOWLEDGMENTS

Z.Z. acknowledges support by NASA through Hubble Fellowship grant HST-HF-51333.01-A awarded by the Space Telescope Science Institute, which is operated by the Association of Universities for Research in Astronomy, Inc., for NASA, under contract NAS 5-26555. We thank Olivier Berné, Simon Casassus and Zsolt Regály for helpful discussions, and Eugene Chiang, the reviewer, for a prompt and constructive report.

REFERENCES

- Adams F. C., Ruden S. P., Shu F. H., 1989, *ApJ*, **347**, 959
- Alexander R., Pascucci I., Andrews S., Armitage P., Cieza L., 2014, *Protostars and Planets VI*, pp 475–496
- Andrews S. M., Wilner D. J., Espaillat C., Hughes A. M., Dullemond C. P., McClure M. K., Qi C., Brown J. M., 2011a, *ApJ*, **732**, 42
- Andrews S. M., Rosenfeld K. A., Wilner D. J., Bremer M., 2011b, *ApJ*, **742**, L5
- Avenhaus H., Quanz S. P., Schmid H. M., Meyer M. R., Garufi A., Wolf S., Dominik C., 2014, *ApJ*, **781**, 87
- Bae J., Hartmann L., Zhu Z., 2015, *ApJ*, **805**, 15
- Bai X.-N., 2015, *ApJ*, **798**, 84
- Baruteau C., Masset F., 2008a, *ApJ*, **672**, 1054
- Baruteau C., Masset F., 2008b, *ApJ*, **678**, 483
- Baruteau C., Papaloizou J. C. B., 2013, *ApJ*, **778**, 7
- Baruteau C., et al., 2014, *Protostars and Planets VI*, pp 667–689
- Benisty M., et al., 2015, *A&A*, **578**, L6
- Birnstiel T., Andrews S. M., Ercolano B., 2012, *A&A*, **544**, A79
- Brown J. M., Blake G. A., Qi C., Dullemond C. P., Wilner D. J., Williams J. P., 2009, *ApJ*, **704**, 496
- Bruderer S., van der Marel N., van Dishoeck E. F., van Kempen T. A., 2014, *A&A*, **562**, A26
- Carmona A., et al., 2014, *A&A*, **567**, A51
- Casassus S., et al., 2013, *Nature*, **493**, 191
- Casassus S., et al., 2015a, *ApJ*, **811**, 92
- Casassus S., et al., 2015b, *ApJ*, **812**, 126
- Crida A., Morbidelli A., Masset F., 2006, *Icarus*, **181**, 587
- Crnkovic-Rubsamen I., Zhu Z., Stone J. M., 2015, *MNRAS*, **450**, 4285
- Espaillat C., et al., 2014, *Protostars and Planets VI*, pp 497–520
- Faure J., Fromang S., Latter H., 2014, *A&A*, **564**, A22
- Flock M., Ruge J. P., Dzyurkevich N., Henning T., Klahr H., Wolf S., 2015, *A&A*, **574**, A68
- Fouchet L., Maddison S. T., Gonzalez J.-F., Murray J. R., 2007, *A&A*, **474**, 1037
- Fukagawa M., et al., 2013, *PASJ*, **65**, L14
- Goodman J., Narayan R., 1988, *MNRAS*, **231**, 97
- Gressel O., Turner N. J., Nelson R. P., McNally C. P., 2015, *ApJ*, **801**, 84
- Heemskerk M. H. M., Papaloizou J. C., Savonije G. J., 1992, *A&A*, **260**, 161
- Hughes A. M., Wilner D. J., Calvet N., D'Alessio P., Claussen M. J., Hogerheijde M. R., 2007, *ApJ*, **664**, 536
- Isella A., Pérez L. M., Carpenter J. M., Ricci L., Andrews S., Rosenfeld K., 2013, *ApJ*, **775**, 30
- Johansen A., Blum J., Tanaka H., Ormel C., Bizzarro M., Rickman H., 2014, *Protostars and Planets VI*, pp 547–570
- Lesur G., Kunz M. W., Fromang S., 2014, *A&A*, **566**, A56
- Lin M.-K., 2012, *MNRAS*, **426**, 3211
- Lovelace R. V. E., Li H., Colgate S. A., Nelson A. F., 1999, *ApJ*, **513**, 805
- Lyra W., Johansen A., Klahr H., Piskunov N., 2009, *A&A*, **493**, 1125
- Lyra W., Turner N. J., McNally C. P., 2015, *A&A*, **574**, A10
- Marino S., Casassus S., Perez S., Lyra W., Roman P. E., Avenhaus H., Wright C. M., Maddison S. T., 2015a, preprint, ([arXiv:1505.06732](https://arxiv.org/abs/1505.06732))
- Marino S., Perez S., Casassus S., 2015b, *ApJ*, **798**, L44
- Masset F., 2000, *A&AS*, **141**, 165
- Masset F. S., 2002, *A&A*, **387**, 605
- Masset F. S., D'Angelo G., Kley W., 2006, *ApJ*, **652**, 730
- Mittal T., Chiang E., 2015, *ApJ*, **798**, L25
- Murray C. D., Dermott S. F., 1999, *Solar system dynamics*
- Owen J. E., Ercolano B., Clarke C. J., 2011, *MNRAS*, **412**, 13
- Paardekooper S.-J., 2007, *A&A*, **462**, 355
- Paardekooper S.-J., 2014, *MNRAS*, **444**, 2031
- Paardekooper S.-J., Mellema G., 2004, *A&A*, **425**, L9
- Paardekooper S.-J., Lesur G., Papaloizou J. C. B., 2010, *ApJ*, **725**, 146
- Papaloizou J. C. B., Pringle J. E., 1984, *MNRAS*, **208**, 721
- Peale S. J., 1993, *Icarus*, **106**, 308
- Pérez L. M., Isella A., Carpenter J. M., Chandler C. J., 2014, *ApJ*, **783**, L13
- Pierens A., 2015, *MNRAS*, **454**, 2003
- Pierens A., Huré J.-M., 2005, *A&A*, **433**, L37
- Piétu V., Guilloteau S., Dutrey A., 2005, *A&A*, **443**, 945
- Pinilla P., Birnstiel T., Ricci L., Dullemond C. P., Uribe A. L., Testi L., Natta A., 2012, *A&A*, **538**, A114
- Regály Z., Juhász A., Sándor Z., Dullemond C. P., 2012, *MNRAS*, **419**, 1701
- Rosenfeld K. A., Chiang E., Andrews S. M., 2014, *ApJ*, **782**, 62
- Takeuchi T., Lin D. N. C., 2002, *ApJ*, **581**, 1344
- Tang Y.-W., Guilloteau S., Piétu V., Dutrey A., Ohashi N., Ho P. T. P., 2012, *A&A*, **547**, A84
- Varnière P., Tagger M., 2006, *A&A*, **446**, L13
- Zhu Z., Stone J. M., 2014, *ApJ*, **795**, 53
- Zhu Z., Nelson R. P., Hartmann L., Espaillat C., Calvet N., 2011, *ApJ*, **729**, 47
- Zhu Z., Nelson R. P., Dong R., Espaillat C., Hartmann L., 2012, *ApJ*, **755**, 6
- Zhu Z., Stone J. M., Rafikov R. R., Bai X.-n., 2014, *ApJ*, **785**, 122
- van Dishoeck E. F., van der Marel N., Bruderer S., Pinilla P., 2015, preprint, ([arXiv:1505.01947](https://arxiv.org/abs/1505.01947))
- van der Marel N., et al., 2013, *Science*, **340**, 1199
- van der Marel N., van Dishoeck E. F., Bruderer S., Pérez L., Isella A., 2015, *A&A*, **579**, A106

This paper has been typeset from a \LaTeX file prepared by the author.